On pulse-to-pulse coupling in low-temperature filamentary plasma-assisted ignition in methane-air flows

PAPER • **OPEN ACCESS**

On pulse-to-pulse coupling in low-temperature filamentary plasma-assisted ignition in methane-air flows

To cite this article: Ravi Patel *et al* 2023 *Plasma Sources Sci. Technol.* **32** 065003

OPEN ACCESS
IOP Publishing
Plasma Sources Science and Technology
Plasma Sources Sci. Technol. **32** (2023) 065003 (17pp)
https://doi.org/10.1088/1361-6595/acd65c

On pulse-to-pulse coupling in low-temperature filamentary plasma-assisted ignition in methane-air flows

Ravi Patel[1,2,*], **Jeroen van Oijen**[2], **Sander Nijdam**[1] **and Nico Dam**[2]

[1] Department of Applied Physics, Eindhoven University of Technology, PO Box 513, 5600 MB Eindhoven, The Netherlands
[2] Department of Mechanical Engineering, Eindhoven University of Technology, PO Box 513, 5600 MB Eindhoven, The Netherlands

E-mail: r.b.patel@tue.nl

Received 4 January 2023, revised 21 April 2023
Accepted for publication 17 May 2023
Published 6 June 2023

Abstract

This work aims to characterize the effects of pulse repetition rate (PRR) and flow speed on dielectric barrier discharge (DBD) plasma pulse-to-pulse coupling and its ability to ignite methane-air flows. Experiments are performed on a homemade DBD flow reactor with 5 mm discharge gap. Pressure and equivalence ratio are kept constant at 700 mbar and 0.6. First, we perform high-speed intensified imaging to visualize pulse-to-pulse plasma behavior and ignition kernel development. In air flows, plasma morphology changes from multiple weak filaments to a few stronger filaments indicating plasma pulse-to-pulse coupling. This leads to plasma energy addition in nearly the same gas volume as the previous discharge. The study performed in methane-air flows highlights the importance of plasma pulse-to-pulse coupling for ignition. We find a critical PRR and a minimum number of pulses required to achieve a strong enough coupling to develop a successful ignition kernel. Ignition probability and kernel growth are also evaluated for various conditions. Finally, plasma pulse-to-pulse coupling is quantified by measuring the plasma parameters such as gas temperature and reduced electric field from an optical emission spectroscopy.

Keywords: nanosecond pulsed DBD plasma, plasma-assisted combustion, plasma spectroscopy

(Some figures may appear in colour only in the online journal)

1. Introduction

Recent developments in pulsed power technology have produced commercial high-voltage sources with nanosecond pulse duration [1]. Repetitive pulses of such short duration allow a high energy loading into plasmas, while also maintaining a high reduced electric field (E/N, with E the electric field and N the gas density) and hence electron temperature (T_e). Typically, nanosecond pulse operated non-equilibrium plasmas have a roughly 100 times higher electron temperature than gas temperature [1–3]. Non-equilibrium chemistry involving high energy electrons creates favourable conditions for chemical processes such as combustion. Combustion is the source of most of the world's energy requirements [4]. In order to minimize the negative impact of combustion on the

* Author to whom any correspondence should be addressed.

environment, it is important to make combustors cleaner and more efficient. One of the possible ways to achieve this is lean combustion. But, ignition and flame stabilization are challenging in lean conditions.

Over the last few decades, plasma-assisted combustion (PAC) has been demonstrated to ignite [5–14] and stabilize [15–21] lean combustion in extreme conditions. Nanosecond repetitively pulsed (NRP) discharges can enhance combustion by generating radicals and heat in nanosecond time scales [22–24]. Through which pathway plasma will enhance the combustion depends on the plasma type and the configuration. At near atmospheric or higher pressures, NRP discharges can have three major forms depending on the operating conditions: (1) corona, (2) glow and (3) spark [25]. The spark regime can be further divided into two sub-regimes. One is a non-equilibrium spark with ionization degree of 10^{-4}–10^{-3} and plasma gas heating on the order of 1000 K per pulse [26]. This regime is also called a transient spark regime. Second is the equilibrium spark regime with gas temperature on the order of 10 000 K and ionization degree close to one [27]. The transition from non-equilibrium to equilibrium spark is very rapid and difficult to control. Minesi *et al* have observed this transition in a 10 ns duration high voltage (HV) pulse [28]. In order to maximize the efficiency of radical production and the non-thermal contribution to combustion enhancement, it is important to maintain the plasma in a non-equilibrium regime. One possible way to achieve this is operating NRP with a dielectric barrier. In typical dielectric barrier discharges (DBDs), one or both electrodes are covered with a dielectric layer [3]. Depending upon the electrode construction and operating conditions, DBDs can be generated in various forms like volumetric diffuse [29, 30], plasma jet [31, 32], filamentary [33, 34] and surface DBDs [35, 36]. DBDs can be operated with alternating or pulsed electric fields [37]. Pulsed DBDs are preferred for chemical activation processes as they enable energy deposition at above breakdown reduced electric field.

Along with the plasma type, the way plasma is introduced to the flame is also a governing factor of PAC pathways. Plasma have been applied upstream of [15, 16], in [19, 38], or downstream of the flame [39, 40]. In recent years, a concept of plasma-assisted ignition-stabilized combustion has been proposed [14, 41–43]. In this concept, plasma is applied upstream of the flame such that it ignites the fuel-air flow repetitively. Such a configuration can stabilize lean combustion beyond blowout limits.

In stagnant conditions, pulsed plasma-assisted ignition has been studied in various forms by several researchers. Cathey *et al* have demonstrated a transient plasma ignitor using a corona discharge [6]. Shcherbanev *et al* have studied surface DBD-assisted ignition in a high-pressure environment [12]. Apart from the above single pulse discharge-assisted ignition studies, nanosecond repetitive-pulse-assisted ignition has been studied by Pancheshnyi *et al* [5]. In NRP discharges, a accumulative effect from multiple pulses is more important as a single pulse is usually not enough to ignite fuel-air mixtures. Depending upon the configuration, energy might be added step-wise in a almost same gas volume which can enhance plasma properties. We define this phenomena as plasma pulse-to-pulse coupling. Lovascio *et al* have studied the effect of pulse repetition rate (PRR) on NRP discharge-assisted ignition in high pressure stagnant conditions [44, 45]. They found an optimal PRR governed by the frequency of flow re-circulation in the discharge gap. Nguyen *et al* have reported the effect of turbulence in similar discharge configuration [46]. For ignition-stabilized combustion, investigation on NRP discharges in flowing fuel-air mixture flows is more important. Extensive work has been reported on NRP DBD plasma-assisted ignition in low pressure (around 100 mbar) conditions [9–11]. However, very few reports are available on NRP discharge-assisted ignition of fuel-air mixture flows at near atmospheric or higher pressure conditions. Lefkowitz *et al* have studied NRP spark discharge assisted ignition in methane-air flows up to 10 m s^{-1} flow speeds. They observe three regimes depending upon flow speeds and PRR: (1) decoupled regime, (2) partially coupled regime, & (3) fully coupled regime. Overall, they found non-monotonous trends in ignition probability with flow speed and PRR variations. These complex trends are governed by PRR, flow residence time between the electrodes, and ignition kernel development time. Depending on these parameters, NRP spark discharges pulse-to-pulse coupling can either create or destroy the ignition kernel [42, 47, 48].

Most of the work reported on NRP discharge-assisted ignition concerns either a full equilibrium plasma regime or non-equilibrium plasma regime with gas heating of more than 1000 K per pulse. In our previous work, we reported that it is possible to maintain NRP discharges below the methane-air auto-ignition temperature and initiate ignition by using DBD [49]. Repetitive ignition dynamics and plasma non-thermal contribution have been investigated as well. We found that plasma pulse-to-pulse coupling is needed for about four consecutive pulses to create a successful ignition kernel at 700 mbar pressure. Various parameters like pressure, equivalence ratio, number of pulses per burst, etc were varied but the study was limited to 150 cm s^{-1} flow speed and 3 kHz PRR. We always achieved ignition at 3 kHz PRR but not always for lower PRR. This leads to a question: is the observation due to plasma-generated active species relaxation timescales or flow residence timescales? With this motivation, we explore the effect of PRR and flow speeds on pulse-to-pulse coupling in NRP DBD and its ability to ignite methane-air flows. First, we present high-speed visualization to characterize pulse-to-pulse coupling in air and methane-air flows. From these measurements, ignition kernel growth rate and critical PRR and minimum number of pulse requirements for ignition are evaluated. Finally, phase-locked optical emission spectroscopy (OES) is performed to quantify the effect of pulse-to-pulse coupling on plasma parameters like gas temperature and reduced electric field.

2. Experimental setup and methods

The flow reactor used in this work is the same as in our previous work. A detailed schematic and more information can be

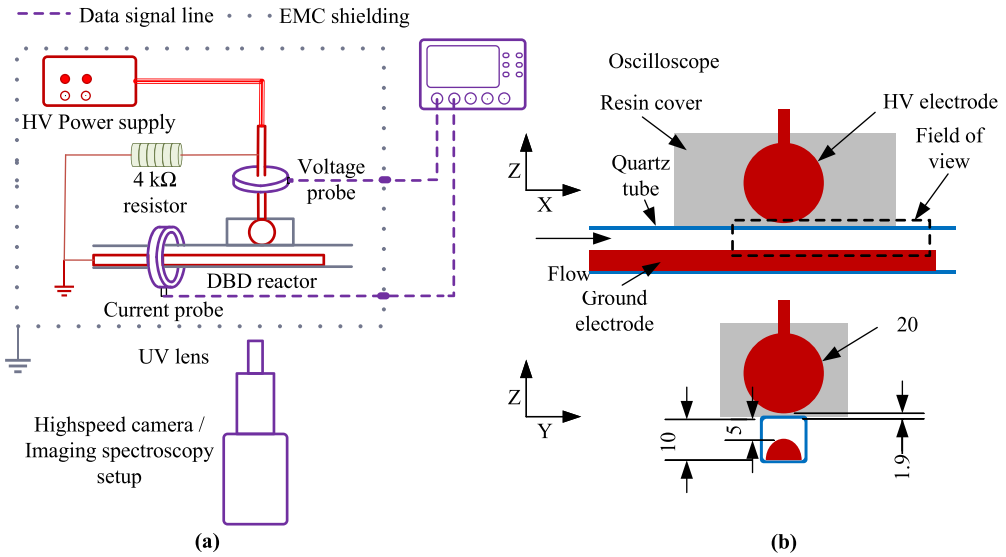

Figure 1. (a) Schematics of the experimental setup and (b) schematics of two side cross-section views of the DBD reactor (all dimensions are in mm). Reproduced from [49]. CC BY 4.0.

found in a previous publication [49]. The reactor is a quartz flow channel with a DBD configuration. Cross-sectional views of the reactor along with the schematics of the overall experimental setup are shown in figure 1.

2.1. DBD reactor configuration

The DBD flow reactor is a quartz tube of 20 cm in length and a square 10 mm by 10 mm cross-section. The HV electrode is placed outside the quartz tube. It is a 20 mm diameter aluminum ball embedded in a resin layer. The grounded electrode is an aluminum rod with a semicircular cross-section which is placed inside the quartz tube. This results in a DBD configuration with a 5 mm discharge gap at the center of the tube and one electrode covered by a 1.9 mm thick dielectric. The setup is built such that pressure and mass flow rate can be varied independently. Mass flow rates are controlled with Bronkhorst mass flow controllers. The pressure is controlled with a vacuum pump, pressure sensor, motorized valve, and PID controller.

In order to investigate the effect of PRR on pulse-to-pulse coupling, we have used a FID 25-10NS10 power supply in this work, which can deliver 10 ns duration HV pulses at up to 30 kHz PRR. A 4 kΩ resistor is connected parallel to the DBD reactor for impedance matching between the power supply and the DBD reactor and to minimize energy coupled during the reflected pulses. The voltage and current waveforms are measured using a homemade D-dot sensor [50] and an AMS CT-F 1.0 S current probe respectively. The D-dot sensor is calibrated with a PVM4 HV probe and was placed on the HV side. The current probe is placed on the ground side. Voltage and current probes have 1 GHz and 500 MHz bandwidths respectively and both waveforms are recorded using a 400 MHz oscilloscope at 5 GSample s^{-1}. High voltage pulses are applied in burst mode in all measurements discussed in this work. The number of pulses per burst and the PRR are varied for parametric studies.

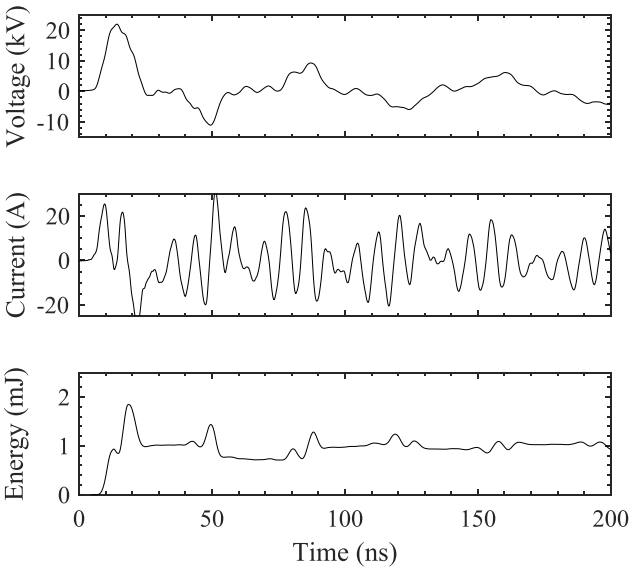

Figure 2. Voltage, current, and energy waveforms from the third plasma pulse in air flow at 700 mbar, 150 cm s^{-1}, and 3 kHz PRR (waveforms are averaged over 100 pulses).

The sample waveforms of the third pulse of a nine pulses burst at 700 mbar, 150 cm s^{-1} flow speed, and 3 kHz PRR are shown in figure 2. The main peak of the voltage waveform has about 10 ns FWHM, 4 ns rise time, and a peak voltage of 21 kV. The first current peak of about 25 A is a capacitive peak which corresponds to the product of the voltage time derivative and the reactor capacitance. The next peak of about 20 A is a resistive peak. This indicates that the plasma breakdown happens on the voltage-falling edge. The instantaneous energy waveform is computed from the measured voltage and current waveforms using

$$E_p = \int v(t) \cdot i(t)\, dt. \quad (1)$$

Most of the energy is coupled during the initial applied voltage peak. The instantaneous energy value then reaches about 1.9 mJ which includes both capacitively and resistively coupled energy. The energy reduces to about 1 mJ once the capacitive energy is reflected back.

2.2. Experimental methods

The experiments performed in this work are centered around two different diagnostic techniques: (1) high-speed imaging of natural luminosity and (2) phase-locked OES. All measurements are performed in burst plasma mode with various number of pulses per burst and various burst frequencies. These conditions are described in the results sections in more detail.

2.2.1. High-speed visualization. High-speed imaging is performed using a combination of a Photron SA-X3 high-speed camera, a La-Vision high-speed intensifier (IRO), and a B-Halle f/2.0 100 nm UV lens. The imaging measurements are performed in two ways for which the timing diagrams are shown in figure 3. The first set of measurements is for pulse-to-pulse plasma visualization for various PRR and flow rate conditions. These are performed with 1 μs exposure time and the camera frame rate identical to the PRR. In this way, we capture emissions following individual plasma pulses in each frame. We also perform single pulse imaging using a PIMAX2 ICCD camera and a 200 mm Nikon camera lens. We achieve better spatial and intensity resolution using this combination because the ICCD camera has 16-bit resolution contrary to the high-speed camera's 12-bit resolution. The higher resolution images are used to obtain the filament's width. Image post-processing is performed in Matlab with the following algorithm. First, the discharge gap is divided into 18 horizontal sections and binned. Then, the binned profiles are fitted with a double Gaussian function. Samples of fitted profiles are given in 'FWHM evaluation of plasma filament'. The FWHMs of these profiles are determined using the Findpeaks function.

The second set of imaging measurements visualises ignition kernel development. The camera exposure time and frame rate are kept constant at 25 μs and 30 kHz, respectively, for all measurements in this set. So, depending upon the PRR, we capture a varying number of frames between two plasma pulses. For example, ten frames are recorded between two plasma pulses for 3 kHz PRR, as illustrated in figure 3(b), whereas only one frame is captured in between two pulses for 30 kHz cases. 300 images per burst are recorded which allows tracking of the kernel up to 10 ms after the burst has started. Ignition kernel growth rates for various conditions are evaluated using a Matlab image processing script. The post-processing script includes three major steps. First, imgaussfilt and imclose filters are applied to the raw image. These filters smoothen the raw image and fill up the inner voids of the ignition kernel images. This was necessary to remove the graininess of the raw signal. The second step is to convert the smoother image to a binary image. The threshold for the binarization was set relative to the maximum intensity of the image. This helps to minimize blooming effects due to image saturation just after the plasma pulses. In the third step, the kernel area and number of kernels are evaluated using Matlab's Regionprops function. In this way, the area is tracked till 10 ms after the burst initiation. A detailed description of the processing script can be found in 'Ignition kernel area evaluation'.

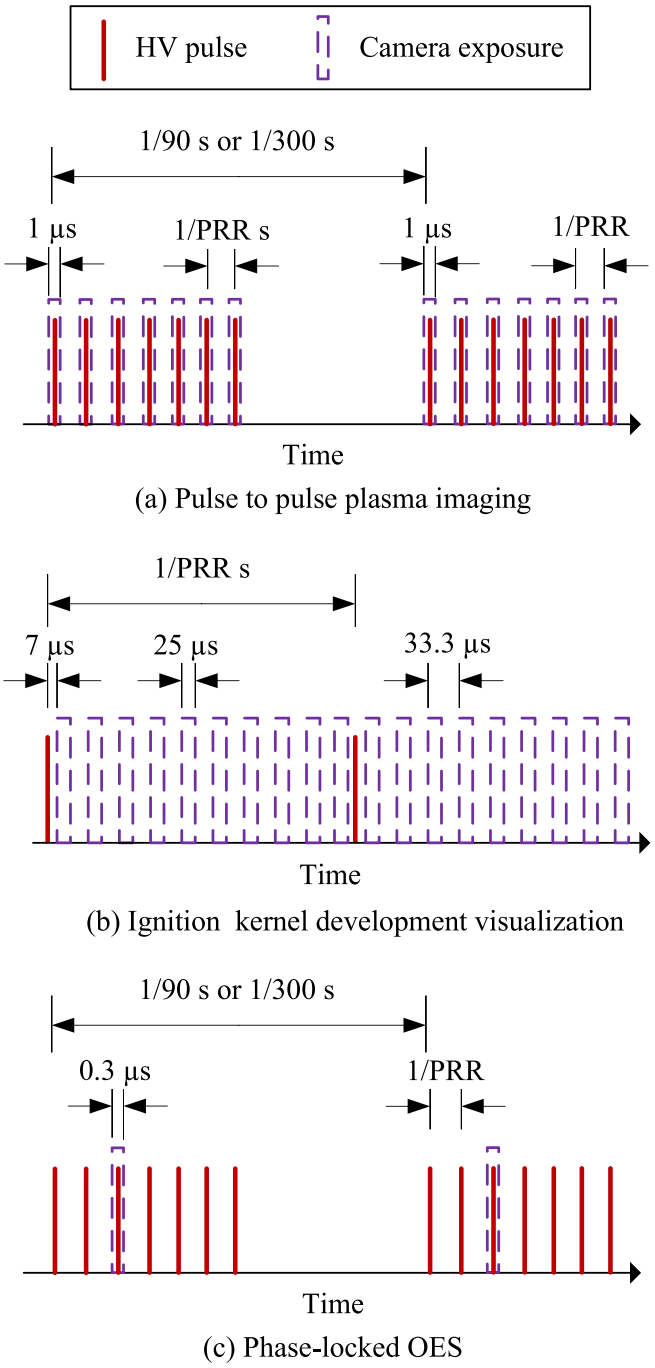

Figure 3. Timing diagrams for (a) pulse-to-pulse plasma imaging, (b) ignition kernel development visualization, and (c) phase-locked optical emission spectroscopy.

2.2.2. OES. Apart from visualization measurements, we have also performed phase-locked OES to quantify plasma properties. For that, a combination of an Acton SP2500

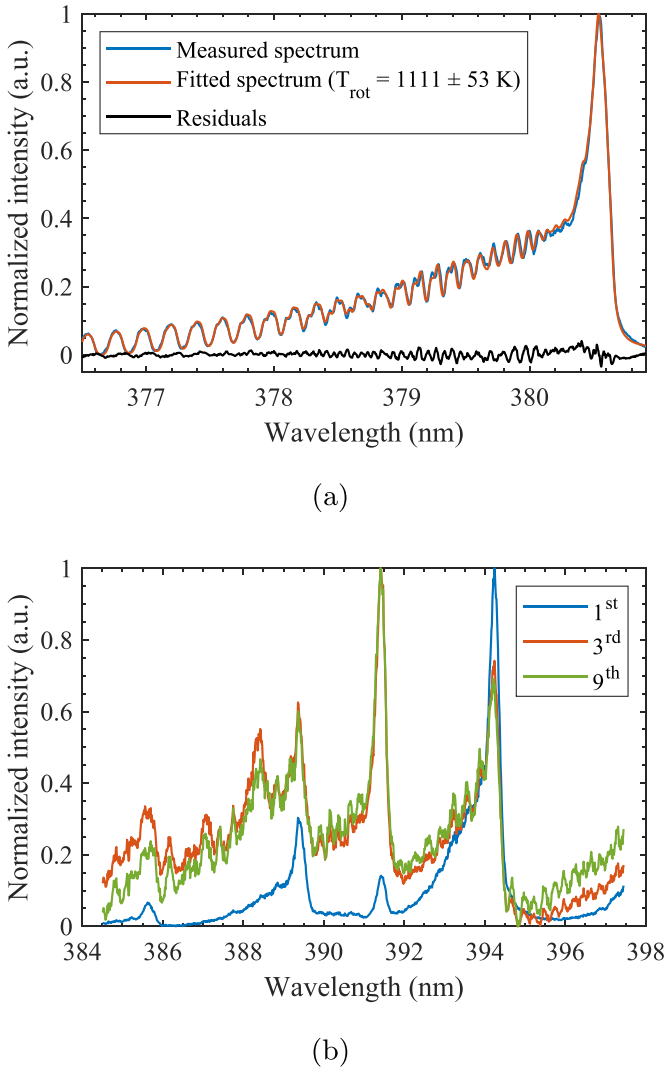

Figure 4. (a) Measured emission spectrum of air plasma with fitted spectrum and residual at 30 kHz PRR, and 150 cm s^{-1} flow speed for the third pulse in a burst and (b) Measured emission spectra of air plasma used for E/N estimations at 30 kHz PRR, and 150 cm s^{-1} flow speed for the first, third and ninth pulse in a burst.

spectrometer, a Princeton instruments PIMAX3 ICCD camera, and a B-Halle f/2.0 UV lens is used. The spectrograph slit was aligned in the direction of the flow. The measurements shown in this work are performed at 1.25 mm above the grounded electrode. A tungsten ribbon lamp is used for the relative intensity calibration of the setup. In figure 1(c), the timing diagram of the phase-locked measurements is shown. Every measurement point is accumulated over 500–1500 shots to collect enough intensity for processing. ICCD gate time is kept to 300 ns. Similar to our previous work, we used the $N_2(C\rightarrow B, \Delta\nu = 1)$ band of the nitrogen second positive system (SPS) for plasma gas temperature estimations, and the intensity ratio of N_2^+(B-X,0-0) and N_2(C-B,5-2) for an effective reduced electric field estimation. $N_2(C\rightarrow B, \Delta\nu = 1)$ spectra were produced using a 3600 grooves mm^{-1} UV grating. The rotational temperature was estimated by fitting the spectra using Massive OES tool [51, 52]. Massive OES software can do batch processing with fit quality estimations. The gas temperature can be assumed to be essentially identical to the rotational temperature as the R-T relaxation timescales are much smaller than the N_2(C) lifetime for the studied operating conditions [53]. Sample of measured and fitted spectra of air plasma at 30 kHz PRR and 150 cm s^{-1} flow speed for the third pulse in a burst is shown in figure 4(a). The N_2^+(B-X,0-0)) peak at 391.4 nm and N_2(C-B,5-2) peak at 394 nm are captured in a single spectrum using a 1800 grooves mm^{-1} grating. A sample spectra of the first, third, and ninth pulses are shown in figure 4(b). The effective reduced electric field is estimated by relating the measured intensity ratio with the empirical relation given by Paris *et al* [54]. The estimated field is spatially averaged over filament width and temporarily averaged over pulse duration. The local instantaneous field can be different from it. The measured spectra are inherently weighted by the emitted light intensity and therefore the combination of local electron density and electric field. Therefore, we believe that the reported values are close to the real peak values during a given pulse number.

3. Results and discussions

The main aim of this work is to characterize the effect of PRR on pulse-to-pulse coupling in a DBD plasma used for PAC. All measurements are performed in burst mode so that each measurement has a well-defined start with a fresh gas mixture. The number of pulses in a burst, the PRR, and the flow speed are varied. Pressure and methane-air mixture equivalence ratio are kept constant at 700 mbar and 0.6 respectively. The 700 mbar pressure was chosen to ensure regular plasma ignition/breakdown. Also, this pressure was studied extensively in our previous work [49]. The number of pulses per burst is varied from 3 to 10 because 3 pulses per burst are required to ensure regular plasma ignition/breakdown and 10 pulses per burst are enough for ignition of methane-air mixtures in most conditions. PRR and flow rate are varied from 1 to 30 kHz and 150 to 500 cm s^{-1} respectively. The flow speed is limited to 500 cm s^{-1} as it is enough to study pulse-to-pulse coupling transitions above 2 kHz PRR. As flow speed is varied, burst frequency is also varied to ensure that each burst is independent from the dynamics of the previous burst. These conditions are summarized in table 1.

As described in the previous section, we performed two major types of characterizations. First, we present the visualization measurements to qualitatively demonstrate pulse-to-pulse coupling in air and fuel-air mixture plasmas. Along with qualitative visualization, we quantify plasma filament width, methane-air ignition probability, and ignition kernel growth. Subsequently, spectroscopy measurements are discussed to quantify pulse-to-pulse coupling in various conditions and its effect on plasma parameters.

3.1. Pulse-to-pulse plasma visualization

3.1.1. Air plasma morphology. Pulse-to-pulse air plasma images for 150 and 500 cm s^{-1} flow speeds and 3 and 30 kHz

Table 1. Different burst frequency and average flow speed combinations used.

No.	Flow speed (cm s^{-1})	Burst frequency (Hz)
(1)	75	45
(2)	150	90
(3)	300	180
(4)	500	300

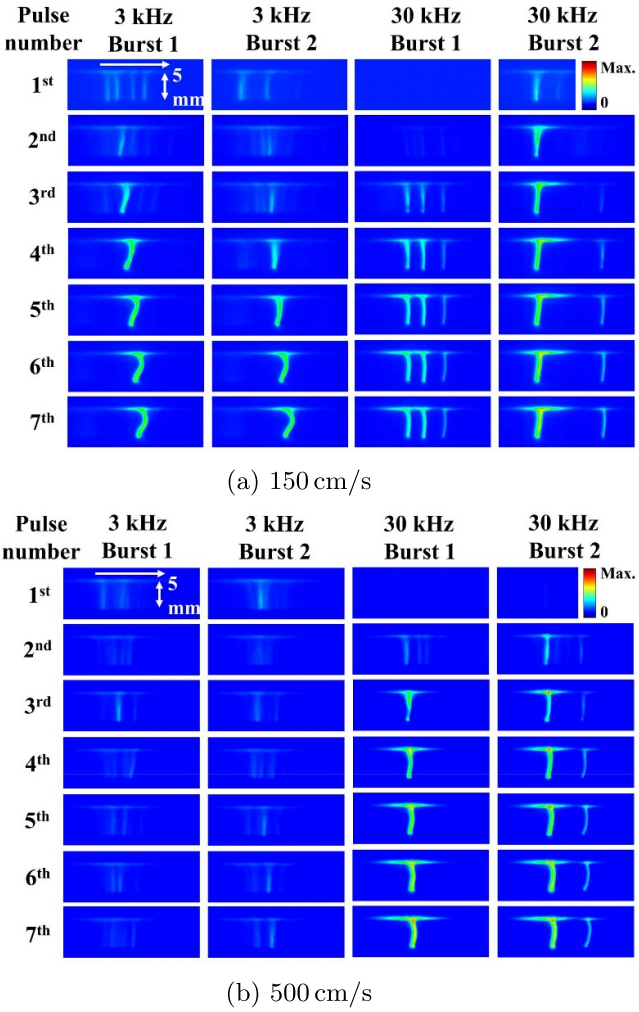

Figure 5. Pulse-to-pulse air plasma discharge images at 700 mbar pressure, 7 pulses per burst and at (a) 150 cm s^{-1} and (b) 500 cm s^{-1} flow speeds. PRR within each burst is indicated above each column and flow direction is from left to right.

PRR are shown in figure 5. Two cases per operating condition are shown. Each burst has seven pulses and the burst frequency is set to 90 Hz. As mentioned in the previous section and shown in figure 3(a), we capture emissions from a single plasma pulse in each frame. Images are presented in false color scale and with a constant intensity scale.

At 3 kHz PRR and 150 cm s^{-1}, multiple weak filaments are seen during the first pulses. After the first pulse, a single filament is seen which becomes brighter from pulse-to-pulse coupling. The observed pulse-to-pulse coupling in the later discharges is quite similar to our previous work in which we highlighted that pulse-to-pulse coupling can be due to residual heat and charge. Long-living negative ions like O^-, O_2^- and charged stored at the dielectric surface can provide free electrons for plasma initiation [2, 3, 55–57]. Once a discharge is initiated, the residual heat can provide an easier path for the discharge. Because the residuals are moving with the flow, filaments also move with the flow. Plasma initiation and pulse-to-pulse coupling during the first three pulses are very weak and not similar for every burst. Contrary, we observed strong coupling from second pulse onwards in previous work [49]. Apart from energy input per pulse, all operating conditions are similar in both cases. The energy input is about 1 mJ per pulse in this work whereas it was about 1.7 mJ per pulse in the previous work. This indicates that lower energy input leads to a weaker plasma and hence weaker pulse-to-pulse coupling. Similar trends are seen for 30 kHz PRR at 150 cm s^{-1} flow speed. Pulse-to-pulse coupling is regular after three pulses. It is important to notice that multiple brighter filaments are often seen for high PRR cases.

At 500 cm s^{-1} flow speed, a similar plasma morphology is seen at 30 kHz PRR, but it is significantly different at 3 kHz PRR. For the latter case, very weak filaments are seen suggesting weaker pulse-to-pulse coupling. From the observations at low flow speeds, we know that pulse-to-pulse coupling is regular only from the fourth pulse. This means that more than four pulses need to be applied to the same gas volume before this gas volume is advected out of the discharge region. The maximum number of pulses for which pulse-to-pulse coupling (n_{pmax}) can be observed depends on the filament residence time inside the DBD geometry. For our reactor configuration, n_{pmax} can be calculated using the following empirically derived equation:

$$n_{\mathrm{pmax}} = 9 \cdot \frac{\mathrm{PRR}}{u_{\mathrm{bulk}}}, \tag{2}$$

where PRR is the PRR in kHz and u_{bulk} is the bulk flow speed in m s^{-1}. The equation is derived from continuous plasma operations. So, it gives a maximum value which is difficult to achieve in burst mode operation. Because the filament is initiated more upstream in the case of continuous mode whereas the initiation location depends on burst-to-burst memory effects for the conditions studied in this work. Equation (2) is explained in more detail in 'n_{pmax} derivation'.

3.1.2. Filament width. Filament width is determined from the ICCD camera images using the method discussed in the previous section 2. In order to visualize pulse-to-pulse effects on filament width in air, normalized intensities of various plasma pulses at 30 kHz PRR and 150 cm s^{-1} flow speed are shown in figure 6(a). For better visualization, 50 shots per case are aligned with respect to the filament center and their normalized average intensity profiles are plotted. During the first pulses, weak but relatively broad filaments are seen while the second pulse filament width is the smallest. From the second pulse, filament width increases with pulse number. The first discharge of a burst occurs in virgin gas with some surface memory effects from the previous burst due to

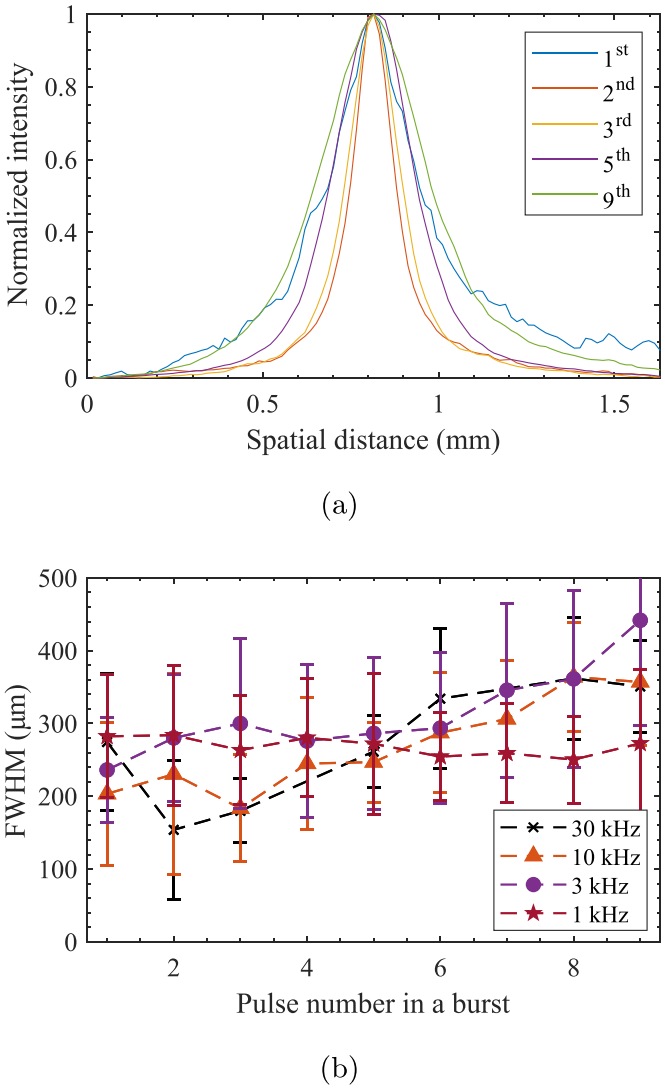

Figure 6. (a) Normalized intensities of air plasma filaments for various pulse numbers in a burst at 30 kHz PRR and 150 cm s^{-1} flow speed and (b) FWHM of these filaments for various pulse numbers and PRR at 150 cm s^{-1} flow speed. These measurements are taken at 1.3 mm above the grounded electrode.

possible charges stored at the dielectric surface. Furthermore, from previous work [49], we know that HV power supplies tend to deliver slightly higher voltages during the first pulse than for the later pulses in a burst. Both of these reasons can lead to a different plasma breakdown mechanism for the first pulse than for later pulses in the burst. For example, Townsend breakdown is seen in atmospheric pressure diffuse DBDs with lower electron impact ionization coefficient and no local field enhancement due to space-charge effects [29, 30].

After the first discharge, plasma breakdown is governed by both volume memory effects and surface memory effects. This leads to plasma energy deposition in almost the same gas volume, as can be seen in figure 5. Thermal and species diffusion in-between plasma pulses can increase the gas volume responsible for the memory effects. Furthermore, elevated temperatures due to pulse-to-pulse coupling will decrease gas density and thereby increase E/N. This can lead to a bigger streamer diameter as less field enhancement at the streamer tip is required for streamer propagation [2]. Mean filament width for various PRR and pulse numbers at 150 cm s^{-1} flow speed is plotted in figure 6(b). Standard deviations are plotted as error bars. For higher PRR, the smallest filaments width is observed after the first pulse and later an increasing trend is seen. This trend is not seen at 1 kHz PRR where pulse-to-pulse coupling is not observed in the high-speed images. Overall, filaments are found to be about 300 μm wide with a large standard deviation (up to 50%). As seen in figure 5, plasma ignition is not similar in every burst which leads to a larger distribution of filament width for the same conditions. Along with this, several mechanisms can contribute to filament widths as explained above, making it very difficult to conclude on the observed trends shown in figure 6. For this, more fundamental research is required. We do not attempt to go in detail as the focus of this work is to analyze plasma ability to ignite fuel-air mixture.

3.2. *Combustion ignition probability*

In this section, we first provide visualization on pulse-to-pulse coupling in methane-air flows and discuss its influence on ignition. As discussed in section 3.1 and shown in figure 3(b), the camera exposures and timing were set such that we capture emissions after the plasma pulses and thereby avoid most plasma emissions. From air plasma images with the same camera settings, we concluded that most plasma emissions last till about 70 μs after the plasma pulse.

High-speed images of methane-air mixtures at 0.6 equivalence ratio, 700 mbar pressure, 3 or 30 kHz PRR, 7 pulses per burst, and 150 or 500 cm s^{-1} flow speed are shown in figure 7. The images show total emission intensities and are in false color scale. As explained above, it can be assumed that the detected signal is mostly combustion chemiluminescence after 70 μs after the plasma pulses. At 3 kHz PRR, ten frames between two plasma pulses are recorded, out of which five images are shown in figures 7(a) and (c). At 150 cm s^{-1} flow speed, we do not detect emissions between the first and second pulses. Two spots are seen after the second pulse which have quenched at 104 μs. These spot's sizes and emission decay times are increased after the third and fourth pulse but still quench before the next pulse. This shows that four pulses are not enough to create a self sustaining ignition kernel. After the fifth pulse, one of the spots survives till the sixth pulse and expands during later pulses. This leads to a successful ignition kernel development which can sustain without plasma support. Further ignition kernel development and kernel size are discussed in the next section. We capture only one frame in-between two pulses at 30,kHz PRR, as PRR and frame rate are the same in this case. Similar to the 3 kHz case, two spot emissions are seen after the second pulse which grow from pulse to pulse. This results in multiple kernel initiations. The kernels' intensities are much brighter because the images are the frames just after the plasma pulses. So, captured intensities are the sum of combustion chemiluminescence and some plasma emissions.

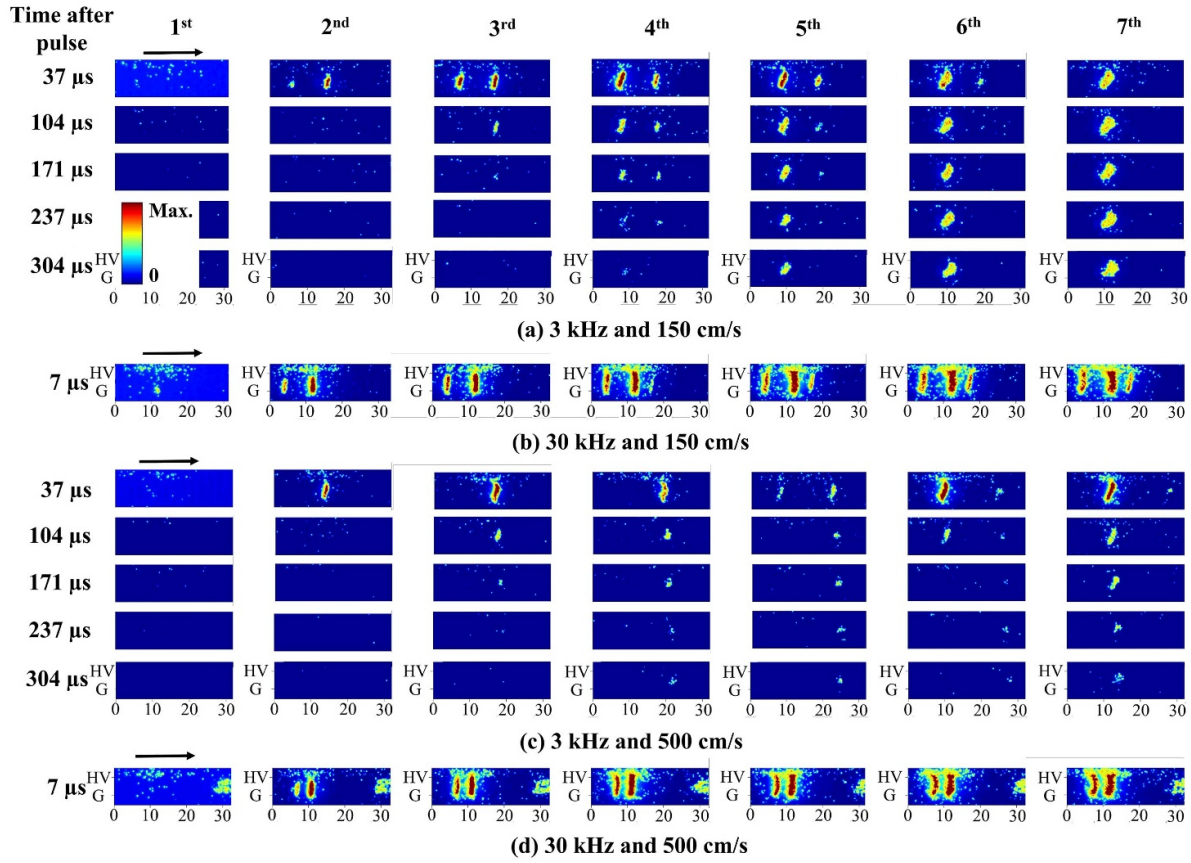

Figure 7. High-speed images of ignition kernel development in methane-air flows at 3 or 30 kHz PRR and 150 or 500 cm s^{-1} flow speed. Dimensions are in mm.

Besides 150 cm s^{-1} flow speed results, 500 cm s^{-1} results are also shown in figure 7. At 3 kHz PRR, self-sustaining ignition kernels are not observed even after seven pulses. Apparently, the high flow speed is limiting pulse-to-pulse coupling in the same kernel volume. We observe similar trends during the first four pulses as for the low flow speed cases. First, a spot-like kernel is created, the decay time of which increases from pulse to pulse. But it is blown out of the discharge zone after five pulses in the high flow speed case, making it weaker while a new spot is created in the discharge zone. Interestingly, at 30 kHz PRR, similar trends are observed for both flow speeds. Here, it is important to note that emission pockets detected at about the 30 mm mark in figure 7(d), are ignition kernels from the previous burst. As burst frequency is increased to 300 Hz for 500 cm s^{-1}, the ignition kernel travels less distance before the next burst is initiated.

From the above results, it is evident that pulse-to-pulse coupling for a certain minimum number of pulses is crucial for successful ignition kernel creation. In order to quantify this phenomenon, successful ignition probability for varying number of pulses is evaluated by analysing more than 60 bursts per condition; the results are plotted in figure 8. 'Successful ignition' is defined as the presence of an expanding ignition kernel after the burst and the 'successful ignition probability' is defined as the ratio between successful ignition bursts and the total number of bursts.

The number of pulses per burst is varied from 3 to 10. A minimum of 3 pulses per burst is required for regular plasma ignition. At 150 cm s^{-1} flow speed, almost no ignition is observed for all PRR cases with three pulses per burst. Ignition probability increases with number of pulses and almost 100% probability is observed from six pulses per burst at 3 kHz or higher PRR. Increasing trends between three to six pulses for various PRR is not monotonously proportional to PRR. This can be attributed to the change in burst-to-burst memory effects for different PRR cases. We explore this coupling in section 3.4. Moreover, ten pulses are required to have over 95% probability at 2 kHz PRR whereas ignition is not observed at all at 1 kHz PRR. n_{pmax} values for respective PRRs are 12 and 6 pulses which means we can not supply enough pulses at 1 kHz to achieve ignition.

At 500 cm s^{-1} flow speed, significantly different trends are seen for 2 and 3 kHz PRR because of lower n_{pmax} values of five and four pulses respectively. Ignition is not observed at 2 kHz and only a maximum of about 35% ignition probability is achieved at 3 kHz. For PRRs above 5 kHz ($n_{\mathrm{pmax}} > 9$), the probability increases with the number of pulses and about eight pulses are required to achieve over 90% successful ignition. Again, the increasing trend is not monotonous with PRR in these cases as well. Overall, we can conclude that a critical PRR value exists at any given flow rate to enable enough pulse-to-pulse coupling which can ignite the fuel-air mixture.

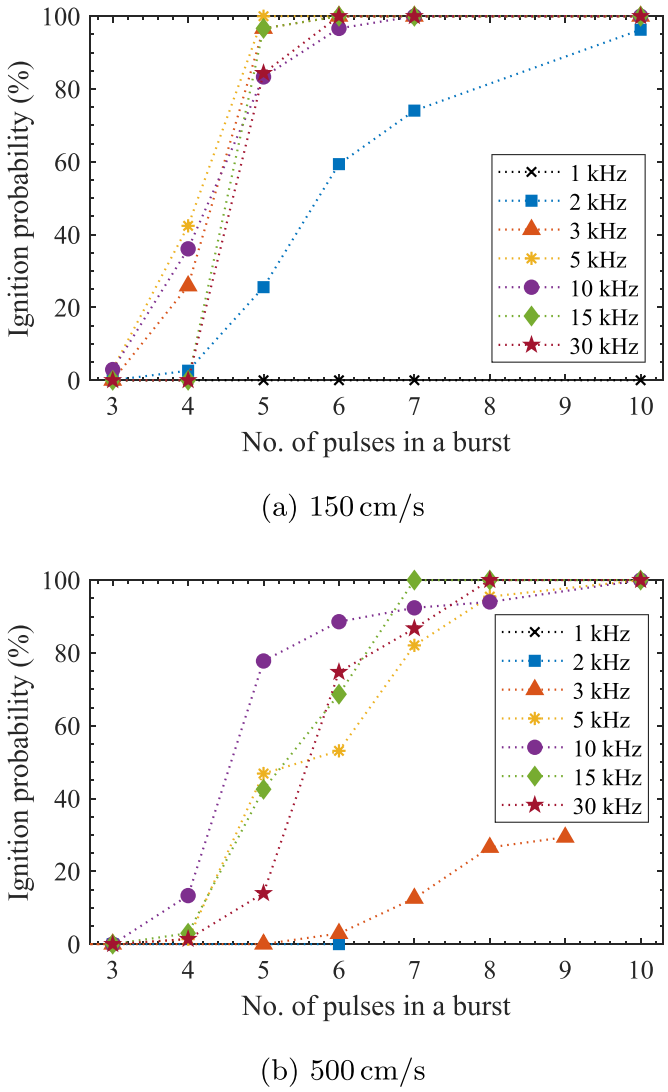

Figure 8. Successful ignition probabilities for various PRR in methane-air flows at 0.6 equivalence ratio, 700 mbar pressure and (a) 150 cm s^{-1} and (b) 500 cm s^{-1} flow speeds.

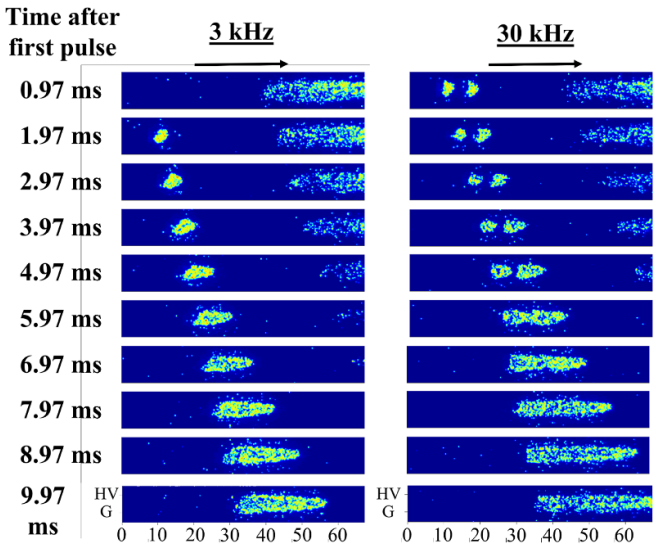

Figure 9. Ignition kernel development visualization at 700 mbar pressure, 150 cm s^{-1} flow speed, 0.6 equivalence ratio, 7 pulses per burst, and at (a) 3 kHz and (b) 30 kHz PRR.

Above this critical PRR, a certain minimum number of pulses should be applied to develop a successful ignition kernel. For examples, the critical PRR and the minimum number of pulses at 150 cm s^{-1} flow speed can be defined as 3 kHz and six pulses. These values increase to 5 kHz and eight pulses at 500 cm s^{-1} flow speed.

3.3. *Ignition kernel growth rate*

In the previous section, we evaluated minimum criteria to ignite the methane-air mixture flows. In this section, we focus on how ignition kernel development is influenced by the conditions above the critical PRR and pulses-per-burst values. Figure 9 provides a visualization of the ignition kernel development from single bursts at 3 kHz and 30 kHz PRR. Flow speed and pulses per burst are identical at 150 cm s^{-1} and 7. At 3 kHz, a single ignition kernel is seen from 1.97 ms which expands while moving with the flow. It is obvious that a kernel is initiated earlier at 30 kHz PRR due to energy loading in a shorter duration. For the burst shown in the figure, two kernels are initiated simultaneously which expand and merge after 5 ms. This leads to a larger kernel size at the end for 30 kHz than for 3 kHz.

Ignition kernel development is quantified by evaluating the kernel area in the time series images. The detailed procedure is explained in 'Ignition kernel area evaluation'. The effect of the number of pulses per burst on ignition kernel development is shown in figure 10. For each condition, about 40 cases with successful ignition are analyzed and averaged. Their mean values are shown as solid lines and their standard deviation is represented by the light blue shades. At 3 kHz PRR cases, a sudden jump in the area size is seen just after each plasma pulses because the signal is too intense in the frames just after the plasma pulses due to plasma emissions. This leads to blooming and over-estimation of the area. We minimize the influence of blooming by adapting the threshold value to the maximum intensity in each frame for the area calculation. In all three cases, almost no area is detected after the first pulse, indicating ignition has not occurred. A small area is detected after the second pulse which goes to zero before the third pulse. However, the area size does not go to zero after the third pulse which shows pulse-to-pulse coupling in ignition kernel development. These trends in the mean area values can be recognized in the image set discussed in section 3.2 and shown in figure 7. After the burst, the kernel area increases monotonically with time. The results are shown till 7 ms. Afterwards, the ignition kernel starts to move out of the camera field of view for both cases. Thus, we define the kernel size at 7 ms as the final kernel size which increases with number of pulses per burst. Moreover, the increment in area size from seven to ten pulses is about a half of the increment seen from five to seven pulses.

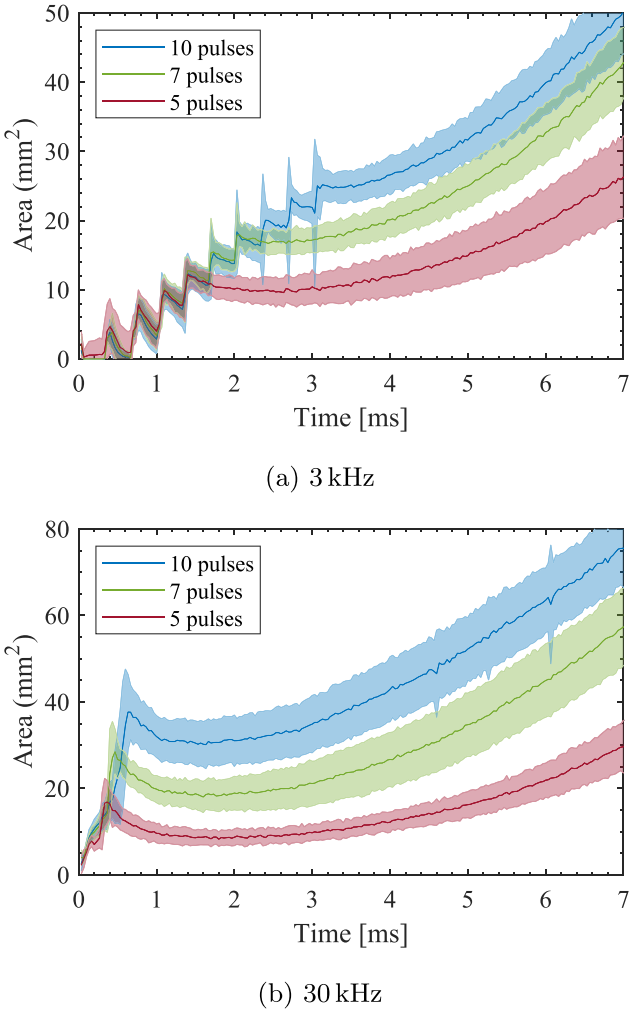

Figure 10. Ignition kernel growth rate in methane-air flows at 700 mbar, 0.6 equivalence ratio, 150 cm s^{-1} flow speed, (a) 3 kHz and (b) 30 kHz PRR and varying number of pulses per burst.

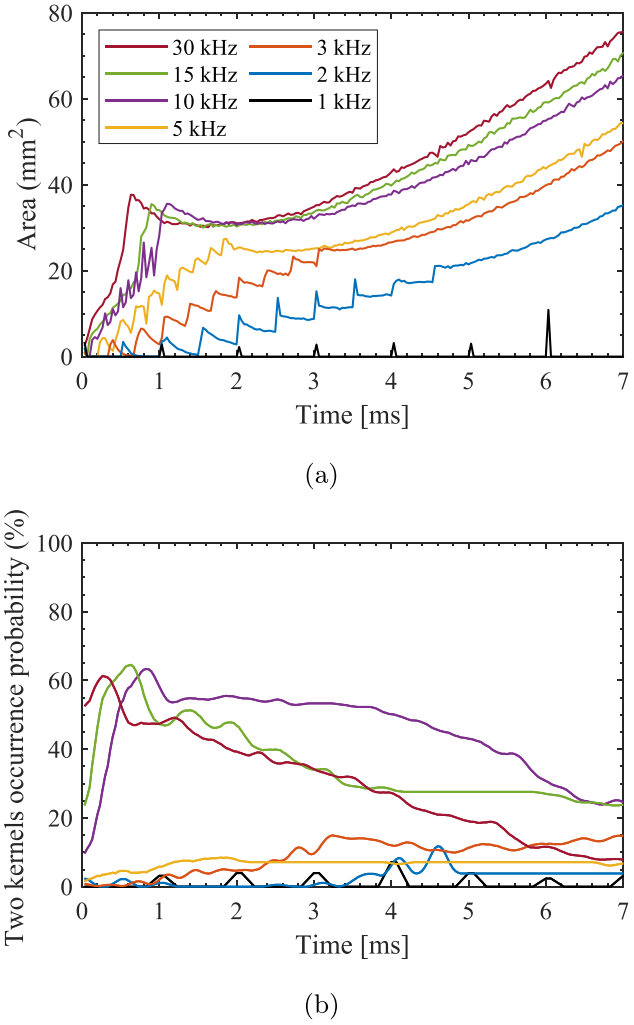

Figure 11. (a) Mean ignition kernel size and (b) probability of occurrence of two ignition kernels in methane-air flows for various PRR and at 700 mbar, 0.6 equivalence ratio, 150 cm s^{-1} flow speed, and 10 pulses per burst.

In contrast to 3 kHz PRR, only one jump in area size is seen at 30 kHz. That is because the frame rate and PRR are identical. Moreover, the increase in area after the burst is much steeper than that at 3 kHz because energy is loaded in a much shorter interval. Although, a small decrease in area is seen at about 1 ms due to blooming. Similar to 3 kHz PRR, the final kernel size increases with number of pulses per burst and increment is smaller for higher numbers of pulses.

Ignition kernel development is compared for various PRRs in figure 11(a). For that, the mean kernel area sizes of the 10 pulses per burst cases at 1 kHz–30 kHz PRR are plotted as a function of time after the start of the burst. Similar to the above experiments, flow speed and equivalence ratio are kept to 150 cm s^{-1} and 0.6. At 1 kHz, we do not observe ignition. Small peaks are seen due to plasma emissions captured in the frames just after the plasma discharges. Similar to the above discussed 3 kHz PRR cases, kernel quenching is seen during first few pulses at 2 kHz as well. A pulse-to-pulse increase in area is seen only after the fourth pulse whereas this is seen from the second pulse at 5 kHz and higher PRR. Initial kernel growth rate during or just after the burst increases with PRR. Obviously, this can be attributed to energy loading on shorter time scales. Moreover, it seems that not only the initial growth rate but also the final kernel size increases with PRR. The final kernel size is much lower at 2 kHz PRR than at 3 or 5 kHz which is again quite smaller than 10–30 kHz PRR. Pulse-to-pulse coupling is weak at 2 kHz and so is the initial growth rate which leads to a lower final kernel size. Furthermore, the larger kernel size at 10–30 kHz is due to the multiple ignition kernel initiations. An example of such a case is already shown in figure 9. The probability of detecting two ignition kernels and their time evolution is plotted in figure 10(b). A five points moving average was applied to smoothen the data. This leads to wider peaks due to plasma emissions at 1 kHz PRR. It is quite evident that two kernels occurrence is much more probable for 10–30 kHz PRRs. Two kernels are initiated in about 60% of the cases; this occurrence decreases in time due to kernels merging or quenching while moving with the flow.

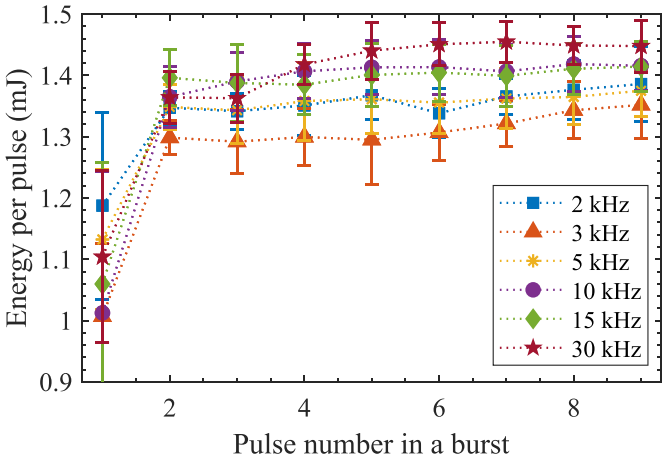

Figure 12. Energy coupled into plasma for various PRR in methane-air flows at 0.6 equivalence ratio and 150 cm s^{-1} flow speed.

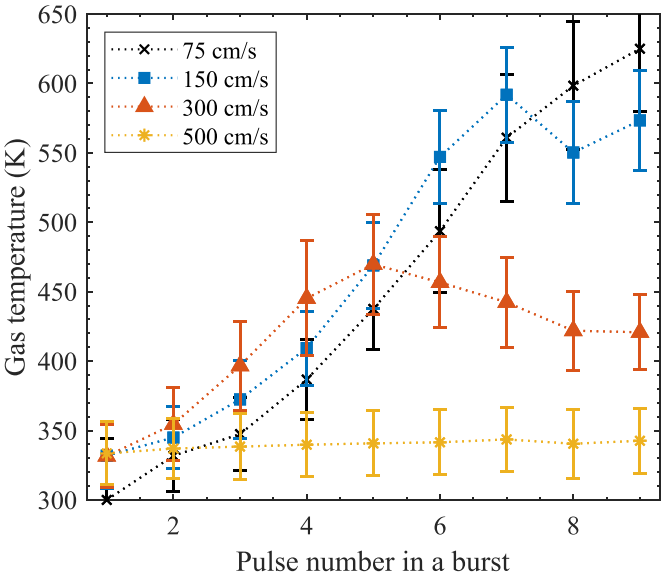

Figure 13. Air plasma pulse-to-pulse gas temperature for various flow speeds at 3 kHz PRR and 700 mbar pressure.

3.4. Plasma parameters

From the above qualitative visualization measurements and quantitative analyses, we learn the importance of pulse-to-pulse coupling in ignition kernel development and the role of the PRR. In order to quantify the effect of PRR on pulse-to-pulse coupling, we have studied the role of three plasma parameters: (1) energy coupled into plasma per pulse, (2) plasma gas temperature, and 3) reduced electric field (E/N).

3.4.1. Energy coupled into plasma. Energy per pulse is calculated from the measured voltage and current waveforms using equation 1. The values are taken after the first main voltage pulse which is at the 40 ns mark in figure 2. In figure 12, the mean energy per pulse for various PRRs in methane-air flows at 150 cm s^{-1} and 0.6 equivalence ratios are plotted. The mean energy values are evaluated by averaging over 50 pulses and their standard deviations are plotted as error bars. Overall, we observe that PRR has no influence on the total energy coupled into the plasma. About 1.4 mJ per pulse energy is measured from the second pulse onwards for all PRRs. The coupled energy during the first pulses is a bit lower due to difficult plasma ignition. In previous work, we reported about 2 mJ per pulse coupled energy in methane-air flows at various pressures. The observation was attributed to almost similar maximum charge storing capacity of dielectric and applied voltage during the breakdown [49]. This is also true for the observed trend for various PRRs. In the previous work, we observed that a minimum of 4 pulses per burst are required to consistently ignite a methane-air flows at 3 kHz PRR and exactly the same other conditions as studied in this work. However, in this work, we observe weaker pulse-to-pulse plasma coupling during the initial three pulses and so more pulses are required for combustion ignition. The difference between both works can be the attributed to the difference of about 0.6 mJ per pulse energy coupling. It will be interesting if we can perform experiments in which energy coupled into plasma can be varied at constant applied E/N. These experiments can help to find an optimal coupled energy per pulse.

3.4.2. Effect of flow on pulse-to-pulse coupling. In order to quantify the effect of flow on pulse-to-pulse coupling, the air plasma gas temperature is compared in figure 13 for various flow speeds and at a constant 3 kHz PRR. As discussed in section 2, the gas temperature is estimated from phase-locked OES. Note that the burst frequency is also increased with flow speed, as mentioned in table 1. In the lowest flow speed case at 75 cm s^{-1}, temperature monotonically increases with pulse number in a burst, whereas, temperature increases till the seventh and fifth pulse number and then decreases for higher flow speeds of 150 and 300 cm s^{-1} respectively. These trends can be attributed to the flow residence time in the discharge region as the gas volume responsible for volume memory effects can be blown out of the discharge region before all HV pulses are delivered at higher flow speeds. At 500 cm s^{-1} flow speed, the pulse-to-pulse temperature rise is not observed indicating no pulse-to-pulse coupling. The ninth pulse temperature decreases with an increase in flow speed whereas this trend is not followed during the initial pulses. Memory effects during the first pulses from the previous bursts are not the same at different flow speeds, as the time between two bursts is varied with flow speeds. Overall, we can conclude that longer residence time leads to more energy addition into the same gas volume and so more pulse-to-pulse temperature rise.

3.4.3. Effect of PRR on pulse-to-pulse coupling. In figure 14, pulse-to-pulse gas temperature in air flows at 150 and 500 cm s^{-1} flow speeds and 1–30 kHz PRR are shown. In air flow at 150 cm s^{-1} flow speed cases, the pulse-to-pulse temperature rise is seen for all PRRs higher than 1 kHz. The pulse-to-pulse temperature rise is higher at higher PRRs even though the energy coupled into the plasma per pulse is almost constant at different repetition rates. This can be attributed to

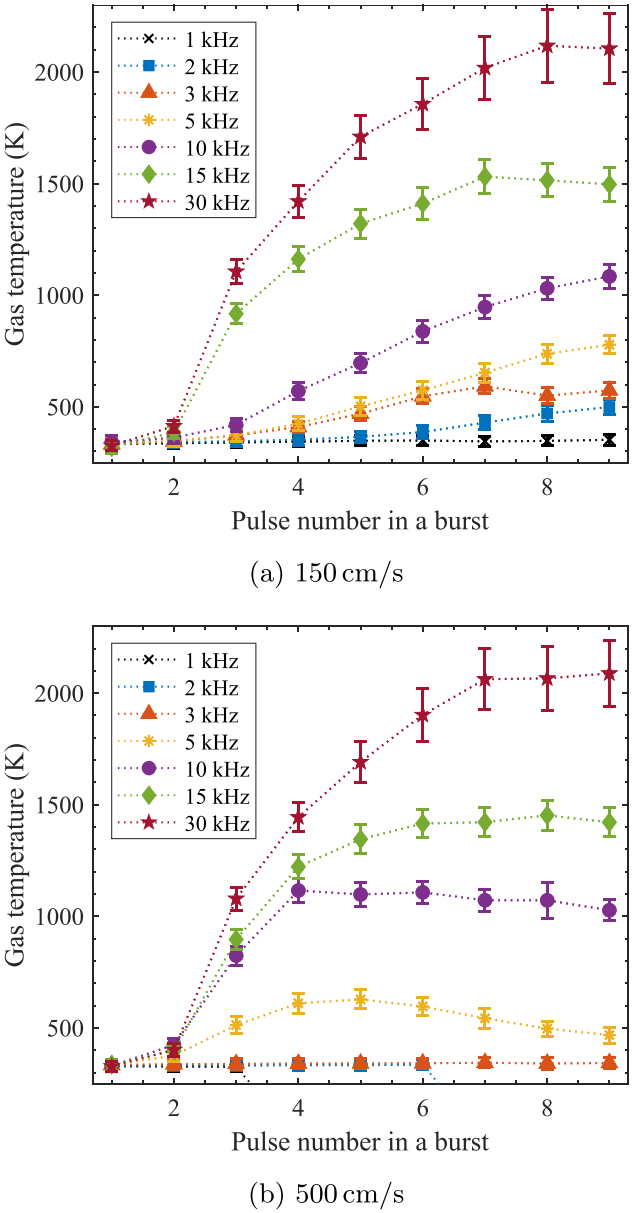

Figure 14. Pulse-to-pulse gas temperature for various pulse repetition rates in air plasma at (a) 150 cm s^{-1} and (b) 500 cm s^{-1} flow speeds.

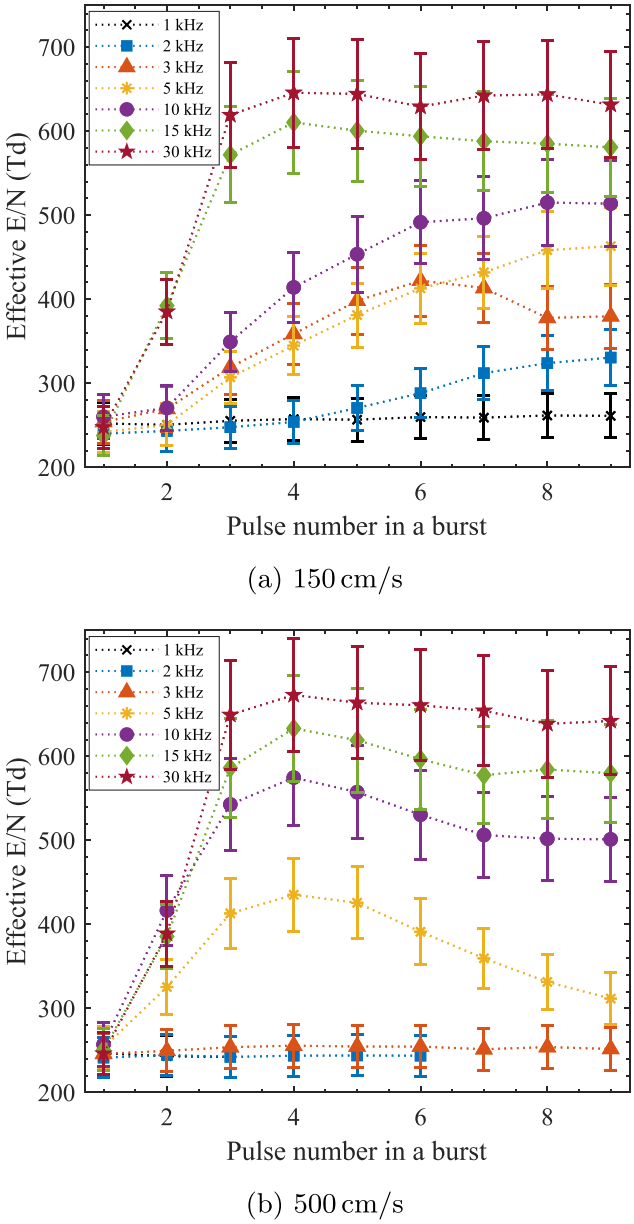

Figure 15. An effective reduced electric field (E/N) for various pulse repetition rates in air flows at (a) 150 cm s^{-1} and (b) 500 cm s^{-1} flow speeds.

the shorter time available for molecular and thermal diffusion in-between plasma pulses at higher PRRs leading to a much stronger pulse-to-pulse coupling.

In air flows at 500 cm s^{-1} flow speed, a similar pulse-to-pulse temperature rise is observed at PRRs above 5 kHz PRR. The temperature reaches about 2000 K at 30 kHz PRR for both flow speeds indicating pulse-to-pulse coupling is not affected by flow speed at higher repetition rates. At slightly lower PRR (5 and 10 kHz), a decreasing trend in temperature is observed from the fifth pulse which we attribute to the effect of flow speed as characterized in the previous section. It is a bit unexpected as $n_{\mathrm{pmax}} \geqslant 9$ for PRR $\geqslant$ 5 kHz. This means that pulse-to-pulse coupling is achieved for much less pulses at high flow speed than the expected value. So, the discharge energy might go into new filament formation after the fifth pulse which can lead to the decrease in temperature. Furthermore, the pulse-to-pulse temperature rise is not observed at 1–3 kHz PRR in high flow speeds cases. These trends are similar to the trends seen in plasma morphology and ignition probability in the previous sections.

For both flow speeds, the air plasma gas temperature is below the methane auto-ignition temperature (870 K [58]) for conditions close to the critical PRRs and minimum number of pulses. This means that the observed ignition is initiated at low-temperature. The conditions above critical PRR and pulses per burst should be avoided as these are prone to plasma NO_x production because of the gas temperature of about 2000 K.

Along with gas temperature, the pulse-to-pulse reduced electric field is also estimated for various PRRs in air

flows and results are plotted in figure 15. At both flow speeds, a pulse-to-pulse increase in E/N is observed following the trends in pulse-to-pulse gas temperature. Pulse-to-pulse increase in gas temperature leads to a lower number density of the gas and so higher E/N. The pulse-to-pulse temperature rise is not observed at or below 1 and 3 kHz PRR for 150 and 500 cm s^{-1} flow speeds, respectively. The effective reduced electric field is measured to be around 240 Td with no pulse-to-pulse increase for these conditions.

4. Conclusions

The effect of PRR on filamentary DBD plasma-assisted ignition in lean methane-air flows is investigated in this work. For that, a flow reactor is used with one electrode covered with dielectric. DBD is operated with 10 ns duration pulses with about 21 kV peak voltage. The measurements are performed in a burst plasma mode with 3–9 pulses per burst and a PRR from 1 to 30 kHz. Pressure and methane-air flow equivalence ratio are kept constant at 700 mbar and 0.6. Various kinds of visualization and spectroscopy measurements are performed to evaluate plasma and combustion ignition properties. From the results, the following conclusions are derived.

Filamentary plasma is observed with about 300 μm FWHM. Filaments become brighter at higher pulse numbers, which is attributed to cumulative plasma energy addition into almost the same gas volume. We call this phenomenon pulse-to-pulse coupling. Pulse-to-pulse coupling leads to a step-wise increase in plasma gas temperature and effective reduced electric field. This coupling becomes stronger at higher PRRs. The pulse-to-pulse coupling plays a crucial role in the ignition of methane-air flows. From parametric visualization measurements, we conclude that there exists a critical PRR and a minimum number of pulses value at a given flow speed to enable strong enough pulse-to-pulse coupling which can create a successful ignition kernel, otherwise a potential kernel quenches quickly after plasma pulses. The critical PRR and the minimum number of pulses both increase with flow speed. We found these values to be 3 kHz and six pulses and 5 kHz and eight pulses for 150 and 500 cm s^{-1} flow speeds. Above these critical values, ignition kernel size increases with the number of pulses per burst and with PRR. The increment in kernel size becomes less at higher PRR and number of pulses per burst.

Furthermore, by comparing results from air plasma temperature measurements and critical conditions required for ignition, we conclude that ignition initiates below the auto-ignition temperature at the conditions close to critical PRR and the minimum number of pulses. The conditions above these critical values should be avoided as the gas temperature goes much higher (about 2000 K), which can lead to significantly higher NO_x production.

Data availability statement

All data that support the findings of this study are included within the article (and any supplementary files).

Table 2. Measured n_{pmax} values for different flow speeds and PRR in continuous plasma operations.

PRR vs u_{bulk}	0.5 m s^{-1}	1 m s^{-1}	2 m s^{-1}
2 kHz	37	15	
3 kHz	59	27	13

Appendix

n_{pmax} derivation

The number of pulses for which pulse-to-pulse coupling (n_{pmax}) can be observed depends on filament residence time in the discharge zone and PRR. Filament residence time depends on filament travel speed (u_{filament}) and distance traveled by the filament in the discharge region (l_{filament}). Simply, it can be formulated as

$$n_{\mathrm{pmax}} = l_{\mathrm{filament}} \cdot \frac{\mathrm{PRR}}{u_{\mathrm{filament}}} \tag{3}$$

l_{filament} is tricky to estimate even though electrode dimensions are known because it is difficult to predict filament initiation location. Moreover, we observe filaments moving in the direction of the flow but the exact relationship between u_{filament} and flow speed is unknown. Also, is it expected that the flow speed varies throughout the discharge region due to a Poiseuille flow profile. Therefore, we used data from pulse-to-pulse imaging in continuous pulsing mode reported in our previous work [49]. The obtained values of n_{pmax} for various conditions are summarized in table 2. From these measured data, we arrived at the following empirical relation:

$$n_{\mathrm{pmax}} = 9 \cdot \frac{\mathrm{PRR}}{u_{\mathrm{bulk}}}, \tag{4}$$

where PRR is in kHz and the bulk flow velocity u_{bulk} is in m s^{-1}. It is important to note here that the equation gives an absolute maximum value which might be difficult to achieve in burst mode operations.

FWHM evaluation of plasma filament

Samples of air plasma filament emission profiles along with fitted Gaussian functions are shown in figure 16. The FWHM of the fitted profiles is taken as the filament width which are 206 and 260 μm for respective cases shown in the figure.

Ignition kernel area evaluation

Ignition kernel growth is evaluated from high-speed chemiluminescence images using image post-processing program in Matlab. It has three major steps. sample images after each processing steps for various instances are shown in figure 18. First, raw images are smoothen using the imgaussfilt and imclose filters. The sigma parameter of the Gaussian filter is kept to 6 and then the image is closed with a disk shaped structure with radius of 6 pixels. In the second step, the filtered image is converted into a binary image. The cutoff for the

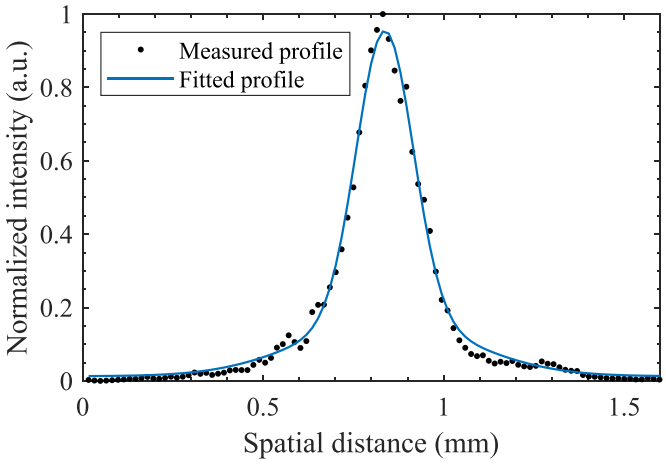

(a) 3^{rd} pulse

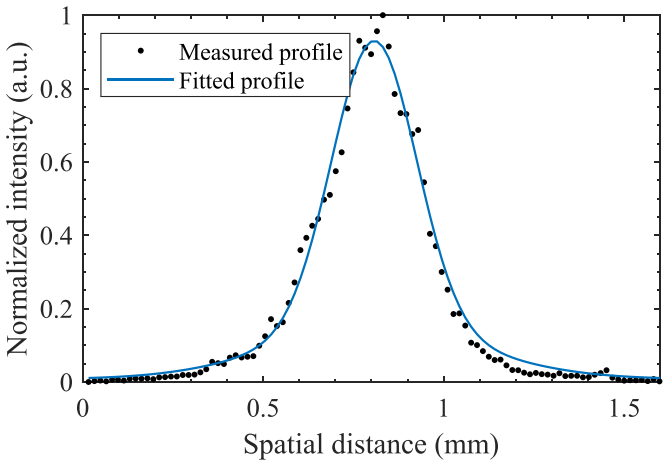

(b) 9^{th} pulse

Figure 16. Measured and fitted profile of air plasma filaments for (a) 3rd pulse and (b) 9th pulse in a burst at 30 kHz PRR and 150 cm s^{-1} flow speed.

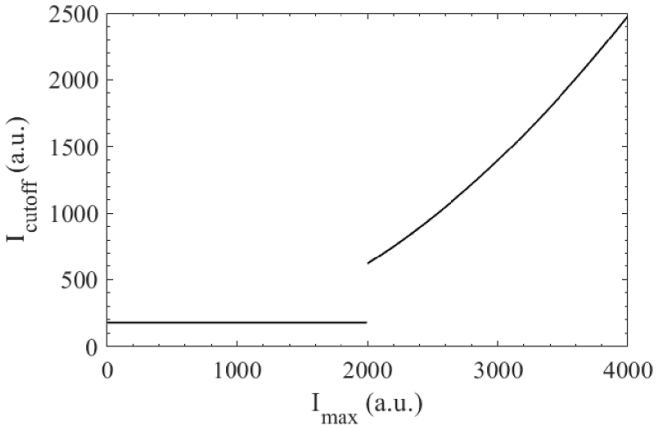

Figure 17. Intensity cutoff I_{cutoff} vs maximum intensity I_{max} relation used for ignition kernel area calculation.

binarization (I_{cutoff}) was set relative to the maximum intensity (I_{max}) of the image. This helps to minimize blooming effects due to image saturation. As it can be seen in figure 18, the maximum intensity is above 2000 counts in images captured just after plasma pulses. Images are even saturated at many of such instances. The relation of the binarization cutoff with

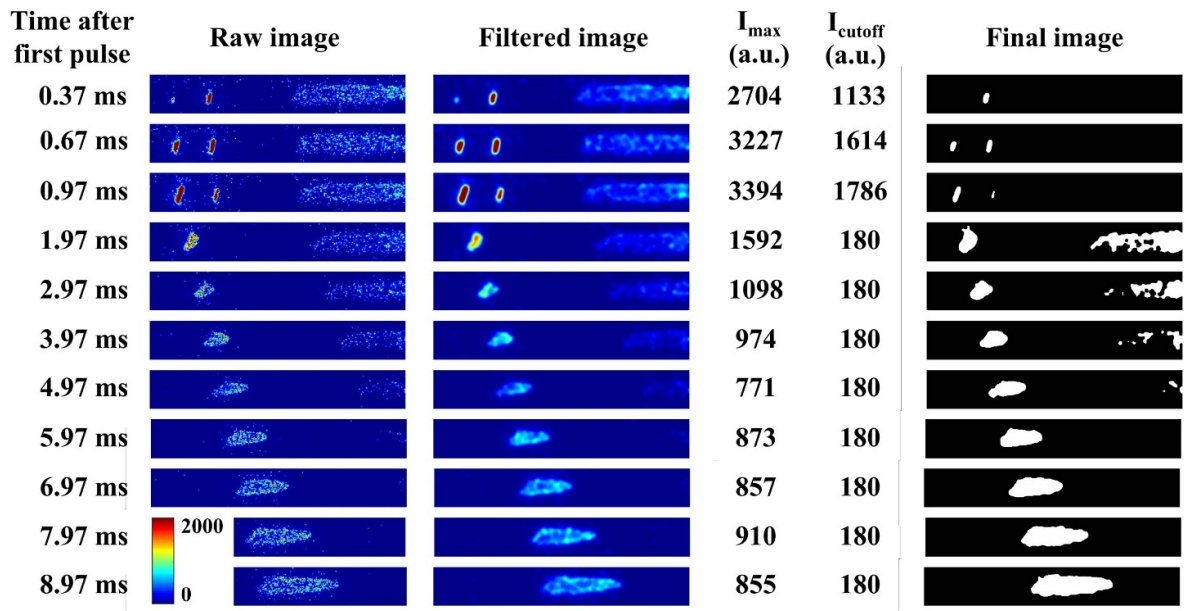

Figure 18. Raw, filtered, and final images used for ignition kernel area calculation along with maximum measured and cutoff intensities at various time instances for methane-air flow at 150 cm s^{-1} flow speed, 0.6 equivalence ratio, 7 pulses per burst, and at 3 kHz PRR.

respect to the maximum intensity is plotted in figure 17. After plasma pulses and ignition kernel development phase, maximum intensity is about 1000 counts. In such cases, the cutoff is kept constant to 180 counts. In the last step, the kernel area, number of kernels, and centroid locations of the kernels are evaluated using the regionprops function. The centroid locations are used to filter out the kernels which were ignited during the previous burst. In this way, the area is tracked till 10 ms after the burst initiation.

ORCID iDs

Ravi Patel https://orcid.org/0000-0002-0117-3339
Jeroen van Oijen https://orcid.org/0000-0002-4283-2898
Sander Nijdam https://orcid.org/0000-0002-1310-6942

References

[1] Huiskamp T 2020 Nanosecond pulsed streamer discharges part I: generation, source-plasma interaction and energy-efficiency optimization *Plasma Sources Sci. Technol.* **29** 023002
[2] Nijdam S, Teunissen J and Ebert U 2020 The physics of streamer discharge phenomena *Plasma Sources Sci. Technol.* **29** 103001
[3] Brandenburg R 2017 Dielectric barrier discharges: progress on plasma sources and on the understanding of regimes and single filaments *Plasma Sources Sci. Technol.* **26** 053001
[4] Turns Stephen R 2000 *An Introduction to Combustion: Concepts and Applications* (Singapore: *McGraw-Hill Companies, Inc*)
[5] Pancheshnyi S V, Lacoste D A, Bourdon A and Laux C O 2006 Ignition of propane–air mixtures by a repetitively pulsed nanosecond discharge *IEEE Trans. Plasma Sci.* **34** 2478–87
[6] Cathey C D, Tang T, Shiraishi T, Urushihara T, Kuthi AAs and Gundersen M A 2007 Nanosecond plasma ignition for improved performance of an internal combustion engine *IEEE Trans. Plasma Sci.* **35** 1664–8
[7] Shiraishi T, Urushihara T and Gundersen M 2009 A trial of ignition innovation of gasoline engine by nanosecond pulsed low temperature plasma ignition *J. Phys. D: Appl. Phys.* **42** 135208
[8] Singleton D, Pendleton S J and Gundersen M A 2010 The role of non-thermal transient plasma for enhanced flame ignition in C_2H_4–air *J. Phys. D: Appl. Phys.* **44** 022001
[9] Lou G, Bao A, Nishihara M, Keshav S, Utkin Y G, William Rich J, Lempert W R and Adamovich I V 2007 Ignition of premixed hydrocarbon–air flows by repetitively pulsed, nanosecond pulse duration plasma *Proc. Combust. Inst.* **31** 3327–34
[10] Bao A, Utkin Y G, Keshav S, Lou G and Adamovich I V 2007 Ignition of ethylene–air and methane–air flows by low-temperature repetitively pulsed nanosecond discharge plasma *IEEE Trans. Plasma Sci.* **35** 1628–38
[11] Lefkowitz J K, Uddi M, Windom B C, Lou G and Ju Y 2015 In situ species diagnostics and kinetic study of plasma activated ethylene dissociation and oxidation in a low temperature flow reactor *Proc. Combust. Inst.* **35** 3505–12
[12] Shcherbanev S A, Stepanyan S A, Popov N A and Starikovskaia S M 2015 Dielectric barrier discharge for multi-point plasma-assisted ignition at high pressures *Phil. Trans. R. Soc.* A **373** 20140342
[13] Nakaya S, Yamaki Y, Ren F and Tsue M 2021 Effects of the discharge frequency on the dielectric barrier discharge ignition behaviors for lean methane–air mixtures at various pressure values *Combust. Flame* **234** 111650
[14] Patel R B, Oommen C and Joy Thomas M 2020 Influence of reduced electric field (E/N) on plasma-assisted low-temperature oxidation *J. Propuls. Power* **36** 235–47
[15] Elkholy A, Shoshyn Y, Nijdam S, van Oijen J A, van Veldhuizen E M, Ebert U and de Goey L P H 2018 Burning velocity measurement of lean methane-air flames in a new nanosecond DBD microplasma burner platform *Exp. Therm. Fluid Sci.* **95** 18–26
[16] Lacoste D A, Moeck J P, Durox D, Laux C O and Schuller T 2013 Effect of nanosecond repetitively pulsed discharges on

the dynamics of a swirl-stabilized lean premixed flame *J. Eng. Gas Turbines and Power* **135** 101501
[17] Paulauskas R, Martuzevičius D, Patel R B, Pelders J E H, Nijdam S, Dam N J, Tichonovas M, Striūgas N and Zakarauskas K 2020 Biogas combustion with various oxidizers in a nanosecond DBD microplasma burner *Exp. Therm. Fluid Sci.* **118** 110166
[18] Di Sabatino F and Lacoste D A 2020 Enhancement of the lean stability and blow-off limits of methane-air swirl flames at elevated pressures by nanosecond repetitively pulsed discharges *J. Phys. D: Appl. Phys.* **53** 355201
[19] Taek Kim G T, Sang Yoo C S, Ho Chung S H and Park J 2020 Effects of non-thermal plasma on the lean blowout limits and CO/NO_X emissions in swirl-stabilized turbulent lean-premixed flames of methane/air *Combust. Flame* **212** 403–14
[20] Takita K, Murakami K, Nakane H and Masuya G 2005 A novel design of a plasma jet torch igniter in a scramjet combustor *Proc. Combust. Inst.* **30** 2843–9
[21] Do H, Cappelli M A and Godfrey Mungal M 2010 Plasma assisted cavity flame ignition in supersonic flows *Combust. Flame* **157** 1783–94
[22] Ju Y and Sun W 2015 Plasma assisted combustion: dynamics and chemistry *Prog. Energy Combust. Sci.* **48** 21–83
[23] Starikovskiy A and Aleksandrov N 2013 Plasma-assisted ignition and combustion *Prog. Energy Combust. Sci.* **39** 61–110
[24] Starikovskaia S M, Kukaev E N, Kuksin A Y, Nudnova M M and Starikovskii A Y 2004 Analysis of the spatial uniformity of the combustion of a gaseous mixture initiated by a nanosecond discharge *Combust. Flame* **139** 177–87
[25] Pai D Z, Lacoste D A and Laux C O 2010 Transitions between corona, glow and spark regimes of nanosecond repetitively pulsed discharges in air at atmospheric pressure *J. Appl. Phys.* **107** 093303
[26] Rusterholtz D L, Lacoste D A, Stancu G D, Pai D Z and Laux C O 2013 Ultrafast heating and oxygen dissociation in atmospheric pressure air by nanosecond repetitively pulsed discharges *J. Phys. D: Appl. Phys.* **46** 464010
[27] Lo A, Cessou A, Lacour C, Lecordier B, Boubert P, Xu D A, Laux C O and Vervisch P 2017 Streamer-to-spark transition initiated by a nanosecond overvoltage pulsed discharge in air *Plasma Sources Sci. Technol.* **26** 045012
[28] Minesi N, Stepanyan S, Mariotto P, Stancu G D and Laux C O 2020 Fully ionized nanosecond discharges in air: the thermal spark *Plasma Sources Sci. Technol.* **29** 085003
[29] Belinger A, Dap S and Naudé N 2022 Influence of the dielectric thickness on the homogeneity of a diffuse dielectric barrier discharge in air *J. Phys. D: Appl. Phys.* **55** 465201
[30] Bílek P, Kuthanová L, Hoder T and Šimek M 2022 Atmospheric pressure Townsend discharge in pure nitrogen–a test case for $\mathbf{N}_2(\mathbf{A}^3\sigma^+{}_u, v)$ kinetics under low E/N conditions *Plasma Sources Sci. Technol.* **31** 084004
[31] Becker K, Koutsospyros A, Yin S M, Christodoulatos C, Abramzon N, Joaquin J C and Brelles-Mariño G 2005 Environmental and biological applications of microplasmas *Plasma Phys. Control. Fusion* **47** B513
[32] Winter J, Brandenburg R and Weltmann K-D 2015 Atmospheric pressure plasma jets: an overview of devices and new directions *Plasma Sources Sci. Technol.* **24** 064001
[33] Brandenburg R, Hoder Taš and Wagner H-E *et al* 2008 Two-dimensional spatially resolved cross-correlational spectroscopy of the microdischarge development in barrier discharges in air *IEEE Trans. Plasma Sci.* **36** 1318
[34] Kozlov K V, Wagner H-E, Brandenburg R and Michel P 2001 Spatio-temporally resolved spectroscopic diagnostics of the barrier discharge in air at atmospheric pressure *J. Phys. D: Appl. Phys.* **34** 3164
[35] Shao T, Jiang H, Zhang C, Yan P, Lomaev M I and Tarasenko V F 2013 Time behaviour of discharge current in case of nanosecond-pulse surface dielectric barrier discharge *Europhys. Lett.* **101** 45002
[36] Dedrick J, Boswell R W, Audier P, Rabat H, Hong D and Charles C 2011 Plasma propagation of a 13.56 MHz asymmetric surface barrier discharge in atmospheric pressure air *J. Phys. D: Appl. Phys.* **44** 205202
[37] Wang Q, Liu F, Miao C, Yan B and Fang Z 2018 Investigation on discharge characteristics of a coaxial dielectric barrier discharge reactor driven by AC and ns power sources *Plasma Sci. Technol.* **20** 035404
[38] Alkhalifa A M, Alsalem A, Del Cont-Bernard D and Lacoste D A 2022 Active control of thermoacoustic fluctuations by nanosecond repetitively pulsed glow discharges *Proc. Combust. Inst.* (https://doi.org/10.1016/j.proci.2022.06.013)
[39] Pilla G, Galley D, Lacoste D A, Lacas F, Veynante D and Laux C O 2006 Stabilization of a turbulent premixed flame using a nanosecond repetitively pulsed plasma *IEEE Trans. Plasma Sci.* **34** 2471–7
[40] Lacoste D A, Xu D A, Moeck J P and Laux C O 2013 Dynamic response of a weakly turbulent lean-premixed flame to nanosecond repetitively pulsed discharges *Proc. Combust. Inst.* **34** 3259–66
[41] Kong C, Li Z, Aldén M and Ehn A 2019 Stabilization of a turbulent premixed flame by a plasma filament *Combust. Flame* **208** 79–85
[42] Lefkowitz J K and Ombrello T 2017 An exploration of inter-pulse coupling in nanosecond pulsed high frequency discharge ignition *Combust. Flame* **180** 136–47
[43] Kong C, Fan Q, Liu X, Ahamed Subash A, Hurtig T, Ehn A, Aldén M and Li Z 2022 Non-thermal gliding arc discharge assisted turbulent combustion (up to 80 kw) at extended conditions: phenomenological analysis *Combust. Sci. Technol.* 1–16
[44] Lovascio S, Ombrello T, Hayashi J, Stepanyan S, Xu D, Daniel Stancu G D and Laux C O 2017 Effects of pulsation frequency and energy deposition on ignition using nanosecond repetitively pulsed discharges *Proc. Combust. Inst.* **36** 4079–86
[45] Castela M, Stepanyan S, Fiorina B, Coussement A, Gicquel O, Darabiha N and Laux C O 2017 A 3D DNS and experimental study of the effect of the recirculating flow pattern inside a reactive kernel produced by nanosecond plasma discharges in a methane-air mixture *Proc. Combust. Inst.* **36** 4095–103
[46] Nguyen M T, Shy S S, Chen Y R, Lin B L, Huang S Y and Liu C C 2021 Conventional spark versus nanosecond repetitively pulsed discharge for a turbulence facilitated ignition phenomenon *Proc. Combust. Inst.* **38** 2801–8
[47] Adams S, Miles J, Ombrello T, Brayfield R and Lefkowitz J 2019 The effect of inter-pulse coupling on gas temperature in nanosecond-pulsed high-frequency discharges *J. Phys. D: Appl. Phys.* **52** 355203
[48] Lefkowitz J K and Ombrello T 2018 Reduction of flame development time in nanosecond pulsed high frequency discharge ignition of flowing mixtures *Combust. Flame* **193** 471–80
[49] Patel R, van Oijen J, Dam N and Nijdam S 2023 Low-temperature filamentary plasma for ignition-stabilized combustion *Combust. Flame* **247** 112501
[50] Huiskamp T, Beckers F J C M, van Heesch E J M and Pemen A J M 2016 B-Dot and D-Dot sensors for (sub)nanosecond high-voltage and high-current pulse measurements *IEEE Sens. J.* **16** 3792–801
[51] Voráč J, Kusýn L and Synek P 2019 Deducing rotational quantum-state distributions from overlapping molecular spectra *Rev. Sci. Instrum.* **90** 123102

[52] Voráč J, Synek P, Potočňáková L, Hnilica J and Kudrle V 2017 Batch processing of overlapping molecular spectra as a tool for spatio-temporal diagnostics of power modulated microwave plasma jet *Plasma Sources Sci. Technol.* **26** 025010

[53] Capitelli M, Ferreira C M, Gordiets B F and Osipov A I 2013 *Plasma Kinetics in Atmospheric Gases* vol 31 (Berlin: Springer)

[54] Paris P, Aints M, Valk F, Plank T, Haljaste A, Kozlov K V and Wagner H-E 2005 Intensity ratio of spectral bands of nitrogen as a measure of electric field strength in plasmas *J. Phys. D: Appl. Phys.* **38** 3894–9

[55] Zhao Z, Huang D D, Wang Y N, Li C J and Li J T 2020 Volume and surface memory effects on evolution of streamer dynamics along gas/solid interface in high-pressure nitrogen under long-term repetitive nanosecond pulses *Plasma Sources Sci. Technol.* **29** 015016

[56] Nijdam S, Takahashi E, Markosyan A H and Ebert U 2014 Investigation of positive streamers by double-pulse experiments, effects of repetition rate and gas mixture *Plasma Sources Sci. Technol.* **23** 025008

[57] Li M, Li C, Zhan H, Xu J and Wang X 2008 Effect of surface charge trapping on dielectric barrier discharge *Appl. Phys. Lett.* **92** 031503

[58] Robinson C and Smith D B 1984 The auto-ignition temperature of methane *J. Hazard. Mater.* **8** 199–203